Propulsion and Energy Forum
July 28-30, 2014, Cleveland, OH
50th AIAA/ASME/SAE/ASEE Joint Propulsion Conference

Modeling and Simulation of EP Plasma Plume Expansion into Vacuum

F. Cichocki, * M. Merino † and E. Ahedo ‡
Universidad Carlos III de Madrid, Av. de la Universidad 30, 28911 Leganés, Spain

Modeling the far region expansion into vacuum of a plume from an electric thruster is crucial in engineering fields such as spacecraft platform design or mission analysis of a novel contactless orbital object relocator technique, known as Ion Beam Shepherd (IBS). In this context, a two-fluid model for the collisionless, quasi-neutral far region plume expansion is presented and two innovative semi-analytical solution methods introduced. A first solution is based on the perturbation method about the hypersonic expansion limit. A second solution, based on the self-similarity assumption, generalizes and contextualizes existing plume models of that kind. The validity and limitations of each approximation are discussed in detail and their accuracy is evaluated by comparing them with the exact solution obtained numerically with the method of characteristics. Lastly, the development plans for an advanced Hybrid/PIC plasma plume simulator, EP2-Plus, are presented.

Nomenclature

c_s	Plasma sonic velocity
e	Electron charge
h	Self-similarity function of the SSM method
M, M_0	Local Mach number and Mach number at the origin
m_i, m_e	Ion and electron mass
n, $\tilde{n}$	Absolute and normalized plasma density number
$\tilde{n}_c$	Axial profile of the normalized plasma density number
n_i,n_e	Ion and electron density number
n_0	Plasma density number at the origin
$\tilde{n}^{(i)}$	i-th order perturbation term of the normalized plasma density number
$\mathcal{P}_e$	Electron pressure tensor
$R_0, \tilde{R}_b$	Normalization radius and normalized 95% ion current beam radius
r, $\tilde{r}$	Radial coordinate and its non-dimensional form
T_e, $\tilde{T}_e$	Electron temperature and its normalized form
T_{e0}	Electron temperature at the origin
$\tilde{u}_c$	Axial profile of the normalized ion axial velocity
$\boldsymbol{u}_i$, $\boldsymbol{u}_e$, $\tilde{\boldsymbol{u}}_i$, $\tilde{\boldsymbol{u}}_e$	Ion and electron mean velocity vector and their normalized forms
u_{i0}	Ion velocity at the origin
u_{zi}, u_{ri}, $u_{\theta i}$	Ion axial, radial and azimuthal velocity
$\tilde{u}_{zi}$, $\tilde{u}_{ri}$	Normalized ion axial and radial velocity
$\tilde{u}_{zi}^{(i)}$, $\tilde{u}_{ri}^{(i)}$	i-th order perturbation term of the normalized ion axial and radial velocity
z, $\tilde{z}$	Axial coordinate and its non-dimensional form
α_0	Divergence angle of the 95% ion current line at the initial plane, equal to $\arctan(\delta(\eta=1))$
α_F	Far field divergence angle of the 95% ion current line
γ	Electron equivalent polytropic cooling exponent

*PhD student, EP2, Departamento de Bioingeniería e Ingeniería Aeroespacial, filippo.cichocki@uc3m.es
†Professor, EP2, Departamento de Bioingeniería e Ingeniería Aeroespacial, mario.merino@uc3m.es
‡Professor, EP2, Departamento de Bioingeniería e Ingeniería Aeroespacial, AIAA senior member, eduardo.ahedo@uc3m.es

δ	Initial radial profile of the divergence angle tangent
ε	Expansion parameter, $\varepsilon = 1/M_0^2$
ϵ_l	Local error in the axial momentum equation for the SSM
ζ	Normalized streamline axial coordinate
η	Normalized streamline radial coordinate or normalized radius at the initial plane
ν	Initial radial profile of the normalized plasma density number
υ	Initial radial profile of the normalized ion axial velocity
ϕ, $\tilde{\phi}$	Electric potential and its normalized form

I. Introduction

The use of electric thrusters in space is experiencing a rapid growth thanks to the large mass savings these thrusters enable with respect to chemical thrusters. Their operation in space results in the generation of a plasma plume, which may interact with the rest of the S/C. Studying the plume expansion in vacuum is therefore crucial in modern S/C platform designs, which must take into account the damaging effects that the extremely fast ions of the plasma beam might have on sensitive S/C surfaces, such as solar panels or optical onboard sensors. Furthermore, the presence of a plasma beam might either induce S/C surface charging or even hinder electromagnetic communications.

The interest in plasma plume expansion has recently increased due to the proposal of an innovative technique for space debris removal known as Ion Beam Shepherd (IBS). The idea here is to de-orbit or re-orbit (to a less populated orbit) a space debris by transferring momentum contactlessly and safely using a plasma beam. Several studies have been carried out on this topic[1–3] and on the related one regarding the use of a plasma beam to deflect an Earth menacing asteroid[4] . More over, a European Commission funded project named *LEOSWEEP* (*Improving Low Earth Orbit Security With Enhanced Electric Propulsion*), has recently started with the goal of demonstrating the technological, economic and legal feasibility of a first low-risk active debris removal mission using the IBS technique as described in Ref. 5.

In order to provide models to cope with the above interest fields, both experiments and numerical simulations are being carried out. Several studies have already characterized experimentally the plume interaction with the S/C and the space environment[6] or the related spacecraft charging phenomena[7] . Nevertheless, such space experiments are very expensive, while ground experiments in vacuum chambers are clearly limited in their prediction efficacy by effects such as the finite chamber size or the residual gas pressure. Hence, the scope of such experiments is still limited to providing crucial data for the fine tuning of numerical plasma plume models, or equivalently an experimental insight on the value of unknown parameters to be used in such models.

Coming to the topic of the plume expansion itself, this is governed by several factors such as the ion kinetic energy, the internal plasma pressure, charge-exchange collisions of ions with neutrals and external electric and magnetic fields. Depending on the distance from the source thruster, such factors have a different relative weight. Very close to the thruster exhaust area (up to a few thruster radii) the predominant effects are those of the local electric fields and of the charge-exchange collisions with the dense neutral cloud surrounding the thruster. This region is usually referred to as *near region plume*. The local electric fields tend to homogenize the plasma plume in space, which typically comes out of the thruster as an ensemble of beamlets (gridded ion thrusters, GIT) or as an annular profile (Hall effect thrusters, HET). Charge-exchange collisions, on the other hand, are responsible for the creation of slow ions, which are strongly affected by the local electric fields and can accumulate on sensitive surfaces or even damage them. Farther away from the thruster, where the plume has already been quasi-neutralized, the environment changes dramatically. Now, the predominant effect is that of the residual plasma pressure, originated by the finite temperature of the neutralizing electrons. This is the so called *far region plume*, in which the radial ambipolar diffusion electric field, generated by the higher electron mobility, makes the local plume divergence increase. The close and far regions of the plume are further illustrated in Fig. 1.

While studying the near region plume clearly requires the use of sophisticated particle based tools, the topic of the far region plume expansion can be studied with a 2-fluids model and partially solved with semi-analytical approximations. An approximation method introduced in this paper is that of expanding the solution in the inverse squared Mach number and will be referred to as the asymptotic expansion method (AEM). Another approach considered represents the generalization of methods based on the self-similarity

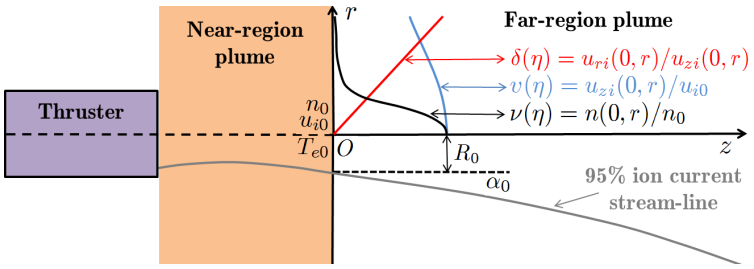

Figure 1. Schematic of a plasma plume and its different regions. The reference plane that serves as the initial condition for the far-region plume is a few thruster radii downstream from the plasma source exit.

assumption (the so-called SSM methods), that were already presented in Refs. 8, 9. Both methods require the definition of some initial beam conditions (initial radial profiles of density and velocity) and of a set of additional assumptions to be verified experimentally. Firstly, the residual electron temperature in the beam has to be specified. Various experiments have been carried out to characterize it, obtaining values ranging from 1 to 5 eV[10,11], being strongly dependent on the neutralizer properties and position with respect to the beam axis. Secondly, it is necessary to define an electrons equation of state. Although some preliminary studies on the collisionless electron cooling in plasma plumes have recently been carried out as described in Refs. 12, 13, in this paper, we shall assume a polytropic law relating temperature and density of the electron cloud. The definition of only one additional parameter is then required: the electron equivalent polytropic cooling exponent γ. Most of the literature currently considers values between 1.0 (isothermal electrons) and 1.4. Beal and Gallimore in Ref. 14 suggest the use of a cooling exponent $\gamma = 1.3$. In general, the higher the γ, the faster the electron temperature drops down and hence the lower the plume divergence growth induced by the electron pressure.

The present work first introduces the fluid equations for the far region plume, which is modelled as a symmetrical, collisionless, quasi-neutral and unmagnetized plasma beam (Sec. II). Then, two semi-analytical methods to obtain an approximated solution are presented: the asymptotic expansion method or AEM (Sec. III) and the self similar method or SSM (Sec. IV). In Sec. V, the accuracy and validity of such methods are then evaluated by comparing their solutions with the numerical solution obtained with the method of characteristics or MOC. Then, both methods are compared in terms of the prediction of the far field divergence angle α_F, an important figure of merit of the plume. The effects of the initial divergence angle α_0, the initial Mach number M_0 or the effective cooling rate γ on this figure of merit are then commented. Finally, the need to extend the simulation capabilities to study more complex phenomena such as the near region plume physics, the plume interaction with external oblique magnetic fields or with a target are justified and the development status of the EP2-Plus code is presented in Sec. VI.

II. Fluid Model for the Far Region Plume

After a distance of a few thruster radii from the thruster exit plane, the plasma jet profile typically becomes single-peaked and smooth, while the near region effects such as collisions with neutrals, neutralizer emissions or the thruster electric and magnetic fields become negligible. Plasma density is already low, typically below 10^{17} m^{-3} and decreasing further downstream, so ion-electron collisional processes can be neglected as well. Lastly, we shall assume that the plasma is quasi-neutral, or equivalently, $n_i = n_e \equiv n$, a condition which can be easily verified close to the thruster exit, where the gradient length (of the order of the thruster radius, $\simeq 10$ cm or larger) is much larger than the Debye length (typically smaller than 1 mm).

In this section we shall introduce the general two-fluid model for this *far region plume*, which will serve as our starting point to derive the semi-analytic approximations of both the AEM and SSM methods. Discarding collisions, ionization/recombination processes and magnetic field effects, the steady-state far-region plume expansion can be macroscopically described by the quasi-neutral fluid equations for singly-charged ions and

electrons:

$$\nabla \cdot (n\boldsymbol{u}_i) = 0, \tag{1}$$

$$\nabla \cdot (n\boldsymbol{u}_e) = 0, \tag{2}$$

$$m_i \left(\boldsymbol{u}_i \cdot \nabla\right) \boldsymbol{u}_i = -e\nabla\phi, \tag{3}$$

$$0 = -\nabla \cdot \mathcal{P}_e + en\nabla\phi, \tag{4}$$

where ϕ is the ambipolar electric potential, n is the quasi-neutral plasma density, and $\mathcal{P}_e$ is the electron pressure tensor, while the rest of symbols are conventional. Note that the ion thermal pressure has been disregarded with respect to electron thermal pressure, as $T_i \ll T_e$ in most plasma plumes. Similarly, electron inertia has been neglected with respect to the electron pressure gradient and the ion inertia.

A kinetic closure is required to model the components of $\mathcal{P}_e$. Solving the plasma plume at a kinetic level is a challenging task beyond the scope of this paper, focussed on the derivation of fast, semi-analytical plume methods. Hence, in the following, we shall approximate $\mathcal{P}_e$ as a diagonal tensor (isotropic), so that $\nabla \cdot \mathcal{P}_e = \nabla p_e$, where $p_e = n_e T_e$ is the scalar electron pressure.

The high conductivity of collisionless electrons suggests a near-isothermal behavior in a large region of the plasma plume, an hypothesis that is supported by several experimental observations[10,11]. This is related to the fact that electrons respond *globally* to the plume expansion and are essentially confined by the potential in the plume, i.e. they can be represented as a cloud with a thermal velocity far larger than the ion drift velocity: $T_e \gg m_e u_i^2$. The isothermal electron assumption, does however lead to the unphysical result of an infinite potential at infinity downstream. Therefore, some collisionless cooling mechanism must exist to gradually lower the electron cloud temperature as the plasma expands. Some experimental evidence shows some degree of cooling in all thrusters, especially in the near region of HETs as found in Ref. 11, 14. Cooling in GIT plumes seems to occur at a much lower pace as suggested in Ref. 15. As mentioned in the introduction, in the absence of an established theory, we shall herein assume a polytropic model for the electrons to account for an effective cooling, i.e. $T_e \propto n_e^{\gamma-1}$. The effective cooling rate can then be tuned with the parameter $\gamma \in [1 \ldots 5/3]$, with $\gamma = 1$ and $5/3$ corresponding respectively to the isothermal and adiabatic cases. Experimental evidence[16,17] seems to suggest values around $\gamma \simeq 1.3$ for HET plumes.

With the above assumptions, density and ion velocity are determined from Eq. (1) together with the plasma (combined) momentum equation,

$$\left(\boldsymbol{u}_i \cdot \nabla\right) \boldsymbol{u}_i = -c_s^2 \nabla \ln n. \tag{5}$$

where $c_s^2 = \gamma T_e / m_i$ is the plasma sonic velocity, which defines the ion Mach number $M = u_i/c_s$.

The plume of existing plasma thrusters (including GITs and HETs) is characterized by electron temperatures T_e in the range 1 to 5 eV and ion velocities u_i between 10 and 50 km/s, corresponding to Mach numbers between 5 and 60. This means that ion motion is highly supersonic (i.e., $M \gg 1$), with the consequence that the resulting ion problem is hyperbolic. Therefore, Eqs. (1) and (5) need to be supplemented with the initial profiles for both the plasma density n and the ion velocity $\boldsymbol{u}_i$ on a reference section downstream of the near-region (e.g. at 0.5 m, where the ion current and plasma density are typically measured in lab experiments). A reasonable choice is a plane $z = 0$ normal to the plume axis. For an axisymmetric, non-rotating plume (i.e. $u_{\theta i}, u_{\theta e} \simeq 0$) and introducing a nomenclature that will become useful later on, we can write these initial conditions in non-dimensional form as:

$$\tilde{n}(0,\tilde{r}) = n(0,\tilde{r})/n_0 = \nu(\eta), \tag{6}$$

$$\tilde{u}_{zi}(0,\tilde{r}) = u_{zi}(0,\tilde{r})/u_{i0} = \upsilon(\eta), \tag{7}$$

$$u_{ri}(0,\tilde{r})/u_{zi}(0,\tilde{r}) = \delta(\eta), \tag{8}$$

with subindex 0 denoting the values of magnitudes at $z = r = 0$, $\tilde{r}$ denoting the radius normalized with a reference radius R_0 (e.g. the initial 95% ion current streamline radius) and η representing this normalized radius at the initial plane. Fig. 1 illustrates these initial profiles.

Applying the same normalization to Eqs. (1) and (5), that is normalizing all variables with their corresponding values at the origin ($\tilde{r} = r/R_0$, $\tilde{z} = z/R_0$, $\tilde{n} = n/n_0$, $\tilde{u}_{zi} = u_{zi}/u_{i0}$, $\tilde{u}_{ri} = u_{ri}/u_{i0}$, $\tilde{T}_e = T_e/T_{e0}$,

$\tilde{\phi} = e\phi/T_{e0}$), we obtain the following non-dimensional equations:

$$\tilde{u}_{zi}\frac{\partial \ln \tilde{n}}{\partial \tilde{z}} + \tilde{u}_{ri}\frac{\partial \ln \tilde{n}}{\partial \tilde{r}} + \frac{\partial \tilde{u}_{zi}}{\partial \tilde{z}} + \frac{1}{\tilde{r}}\frac{\partial (\tilde{r}\tilde{u}_{ri})}{\partial \tilde{r}} = 0, \tag{9}$$

$$\tilde{u}_{zi}\frac{\partial \tilde{u}_{zi}}{\partial \tilde{z}} + \tilde{u}_{ri}\frac{\partial \tilde{u}_{zi}}{\partial \tilde{r}} = -\frac{\tilde{n}^{\gamma-1}}{M_0^2}\frac{\partial \ln \tilde{n}}{\partial \tilde{z}}, \tag{10}$$

$$\tilde{u}_{zi}\frac{\partial \tilde{u}_{ri}}{\partial \tilde{z}} + \tilde{u}_{ri}\frac{\partial \tilde{u}_{ri}}{\partial \tilde{r}} = -\frac{\tilde{n}^{\gamma-1}}{M_0^2}\frac{\partial \ln \tilde{n}}{\partial \tilde{r}}, \tag{11}$$

where the dependency on the main non-dimensional parameter $M_0^2 = m_i u_{i0}^2/(\gamma T_{e0})$ is explicit and the electron cooling effects appear only through the $\tilde{n}^{\gamma-1}$ factors in Eqs. (10) and (11).

Lastly, observe that once $\tilde{n}$ has been computed, Eq. (4) can be used to obtain $\tilde{\phi}$. For an isothermal plasma, we would get:

$$\tilde{\phi} = \tilde{\phi}_0 + ln\,(\tilde{n})\,, \tag{12}$$

where $\tilde{\phi}_0$ is the arbitrary value of the potential at the origin, which can be considered 0 without loss of generality. Additionally, with sufficient boundary conditions, Eq. (2) can then be used to compute $\boldsymbol{u}_e$, which is nevertheless secondary in interest for most applications, in which the absence of electric currents leads to $\boldsymbol{u}_e \simeq \boldsymbol{u}_i$ as a first approximation. A notable exception are thrusters with a magnetic nozzle[18,19], such as the helicon plasma thruster[20,21], where local electric currents (and the magnetic field) can be a dominant feature of the expansion[22] (in particular, the azimuthal ones that have been disregarded here).

The resulting model can then be solved numerically with the method of characteristics (MOC). In the meridional plane, ion equations present three families of characteristic lines: two Mach lines, and the ion streamline. The slopes of these lines are known from the plasma properties. Numerically, the initial plasma front is discretized in a number of nodes, and the characteristic lines are propagated forward and intersected to calculate a new plasma front. The quality of the solution can be improved using a predictor-corrector integration scheme that recalculates the slopes and the new point iteratively. The numerical solution obtained in this way is supported by the physical meaning of the characteristics, and yields very high accuracy with a low computational cost. In the following sections, the MOC solution, calculated with an adapted version of our DIMAGNO code for magnetic nozzles[18], is used to compare and benchmark the semi-analytic approximations to be derived.

It is worth pointing out that the behavior of plume divergence is encapsulated in the M_0 parameter, which measures the relative importance of ion kinetic energy with respect to electron thermal energy, or, in other words, the beam acceleration potential with respect to the electron temperature. For a given initial divergence, a higher M_0 means a smaller role of the electron pressure, which always exerts a radial expanding force on the beam, and hence a lower growth of the divergence angle. On the contrary, low Mach numbers (say < 5) mean that the plasma is still relatively hot: the ions will continue to accelerate as the electrons create an ambipolar electric field that pushes them downstream, while the beam divergence angle will increase substantially.

Before proceeding with the derivation of the semi-analytical methods, two comments on these equations are due. Firstly, note that the system formed by Eqs. (9)–(11) is analogous to the fluid equations of a single neutral, non-viscid species expanding into vacuum. The role of the pressure gradient collisional force of the neutral gas case, is here taken by the ambipolar electric field. Thus, the methods to be presented are equally applicable to the neutral gas expansion case when the same conditions are satisfied. Secondly, observe that a plasma plume model with non-negligible ion temperature that abides by the same thermodynamic assumptions as electrons and shares the same parameter γ can be immediately reduced to the model presented above by redefining the effective temperature and potential as $\tilde{T}_e = \tilde{T}_i + \tilde{T}_e$ and $\nabla\tilde{\phi} = \nabla\tilde{\phi} + \gamma\tilde{T}_i\nabla \ln \tilde{n}$.

III. Asymptotic Expansion Method (AEM)

A first approach to reduce the fluid model of Sec. II to a simple analytical expression is to neglect the pressure term completely, which is equivalent to taking the $M_0 \to \infty$ limit. In this cold plasma limit, the plasma momentum equations Eqs. (10) and (11) (with the right hand side equal to zero) decouple from the continuity equation Eq. (9) to provide the cold-limit velocity field $\tilde{\boldsymbol{u}}_i^{(0)}$. The method only depends on the initial plasma profile functions, ν, υ and δ, and the three characteristic line families collapse into one (the ion streamlines). Observe also that no electric potential builds up in this case: $\tilde{\phi}^{(0)} = 0$.

It follows that $\tilde{\boldsymbol{u}}_i^{(0)}$ is conserved along the streamlines, which are straight rays projected from the initial plane with radius:

$$\tilde{r} = \eta + \delta(\eta)\tilde{z}, \tag{13}$$

and can be labeled by η, their radial position at the initial plane ($\tilde{z} = 0$). Thus, determining the $\eta = \eta(\tilde{z}, \tilde{r})$ map, implicitly given by the equation above, immediately yields $\tilde{u}_{zi}^{(0)}(\tilde{z}, \tilde{r})$ and $\tilde{u}_{ri}^{(0)}(\tilde{z}, \tilde{r})$ from the initial plasma profile.

This map can be understood as the transformation of the reference system $(\tilde{z}, \tilde{r})$ into the new reference system (ζ, η), where simply $\zeta = \tilde{z}$. Differentiation in Eq. (13) provides the Jacobian matrix J of the transformation:

$$J = \begin{bmatrix} \partial\tilde{z}/\partial\zeta & \partial\tilde{r}/\partial\zeta \\ \partial\tilde{z}/\partial\eta & \partial\tilde{r}/\partial\eta \end{bmatrix} = \begin{bmatrix} 1 & \delta \\ 0 & 1 + \zeta\delta' \end{bmatrix} \tag{14}$$

Expressing Eq. (9) in the new coordinates and integrating each streamline along ζ yields the final result for the density:

$$n^{(0)}(\zeta, \eta) = \frac{\nu}{(1 + \zeta\delta')(1 + \zeta\delta/\eta)}, \tag{15}$$

where the prime denotes derivation of the single-variable function δ with respect to η. Eq. (15) reflects the decrease in density as the streamlines diverge $(1 + \zeta\delta')$ and their radius increases $(1 + \zeta\delta/\eta)$.

This cold beam method, while extremely simple, can be used to provide a fast first estimate of plasma density and ion current in the far region from an initial measured or simulated profile, treating the plume as a cone. Clearly, the *local* error committed in the momentum equations is of the order $1/M_0^2$, while the global error (the accumulated integration error, i.e. the difference at each point between the exact solution and the approximation) grows with the distance from the initial plane.

Note that this method requires $\delta, \delta' \geq 0$ to ensure a clean solution exists everywhere. Were such a condition not met, streamlines would eventually cross, with density gradients going to infinity locally, a symptom that pressure effects cannot be neglected around that point.

The method presented above can be regarded as the zeroth-order solution of the hypersonic plume when the variables are expanded in the small parameter $\varepsilon = 1/M_0^2$, i.e.:

$$\begin{aligned} \tilde{u}_{zi} &= \tilde{u}_{zi}^{(0)} + \varepsilon\tilde{u}_{zi}^{(1)} + \varepsilon^2\tilde{u}_{zi}^{(2)} + \dots, \\ \tilde{u}_{ri} &= \tilde{u}_{ri}^{(0)} + \varepsilon\tilde{u}_{ri}^{(1)} + \varepsilon^2\tilde{u}_{ri}^{(2)} + \dots, \\ \ln\tilde{n} &= \ln\tilde{n}^{(0)} + \varepsilon\ln\tilde{n}^{(1)} + \varepsilon^2\ln\tilde{n}^{(2)} + \dots, \end{aligned} \tag{16}$$

where all terms of order one or larger are zero at the initial plane, but grow gradually downstream. The quality of the cold beam solution can be improved by including one or more of these corrections, which allow reducing the local error to $O\left(M_0^{-4}\right)$ (for the first order), $O\left(M_0^{-6}\right)$ (second order), etc. Luckily, momentum and continuity equations remain decoupled at all orders and can be readily integrated *along the zeroth-order streamlines*, requiring only to calculate the gradients of already-known magnitudes.

The first-order correction for the velocity is given by the plasma momentum equations at order ε:

$$\upsilon\frac{\partial\tilde{u}_{zi}^{(1)}}{\partial\zeta} = \frac{\upsilon'}{1 + \zeta\delta'}\left(\tilde{u}_{zi}^{(1)}\delta - \tilde{u}_{ri}^{(1)}\right) - \left(\tilde{n}^{(0)}\right)^{\gamma-1}\left(\frac{\partial\ln\tilde{n}^{(0)}}{\partial\zeta} - \frac{\delta}{1 + \zeta\delta'}\frac{\partial\ln\tilde{n}^{(0)}}{\partial\eta}\right), \tag{17}$$

$$\upsilon\frac{\partial\tilde{u}_{ri}^{(1)}}{\partial\zeta} = \frac{(\upsilon\delta)'}{1 + \zeta\delta'}\left(\tilde{u}_{zi}^{(1)}\delta - \tilde{u}_{ri}^{(1)}\right) - \left(\tilde{n}^{(0)}\right)^{\gamma-1}\frac{1}{1 + \zeta\delta'}\frac{\partial\ln\tilde{n}^{(0)}}{\partial\eta}, \tag{18}$$

where ζ and η are the zeroth order streamline coordinates. Note that $n^{(0)}$ and its derivatives in ζ and η are known analytically from Eq. (15). Once $\tilde{\boldsymbol{u}}_i^{(1)}$ is known, the first-order correction to density is then given by Eq. (9) at order ε:

$$\begin{aligned} \upsilon\frac{\partial\ln\tilde{n}^{(1)}}{\partial\zeta} = &-\tilde{u}_{zi}^{(1)}\left(\frac{\partial\ln\tilde{n}^{(0)}}{\partial\zeta} - \frac{\delta}{1 + \zeta\delta'}\frac{\partial\ln\tilde{n}^{(0)}}{\partial\eta}\right) - \tilde{u}_{ri}^{(1)}\left(\frac{1}{1 + \zeta\delta'}\right)\frac{\partial\ln\tilde{n}^{(0)}}{\partial\eta} \\ &- \frac{\partial\tilde{u}_{zi}^{(1)}}{\partial\zeta} + \frac{\delta}{1 + \zeta\delta'}\frac{\partial\tilde{u}_{zi}^{(1)}}{\partial\eta} - \frac{1}{1 + \zeta\delta'}\frac{\partial\tilde{u}_{ri}^{(1)}}{\partial\eta} - \frac{\tilde{u}_{ri}^{(1)}}{\eta + \zeta\delta} \end{aligned} \tag{19}$$

Again, it is important to notice that, in spite of the apparently cumbersome expression, all derivatives are analytically known, except for those of velocity along η, which can be easily computed by numerically differentiating known magnitudes.

The same procedure can be applied to easily obtain higher-order corrections. Unfortunately, the non-linearity introduced by the ion convective term means that all previous-orders in the velocity contribute to higher-order corrections. Likewise, the $\tilde{n}^{\gamma-1}$ term means that all previous-order density corrections determine the next-order correction in non-isothermal cases, according to the expansion:

$$\left(\tilde{n}^{(i)}\right)^{\varepsilon^i(\gamma-1)} = 1 + \varepsilon^i(\gamma-1)\ln\tilde{n}^{(i)} + \dots \tag{20}$$

Fig. 2(a) shows the initial profiles used, which have 95% of the ion current within the streamline $\eta = 1$ and a divergence angle α_0 of 20 deg for this streamline. A Gaussian density profile has been assumed, while axial velocity and divergence profile resemble those a conical beam expansion with a constant total velocity (several HET plume experiments seem to suggest such a velocity profile). Fig. 2(b) shows the corresponding plasma density contour lines and the 95% ion current streamline ($\eta = 1$) for a $M_0 = 30$ flow. Clearly, the first order streamlines tend to expand radially at the beginning and the consequence is that the first order density along the centerline is lower than the zeroth order one, while it is higher in the plume periphery.

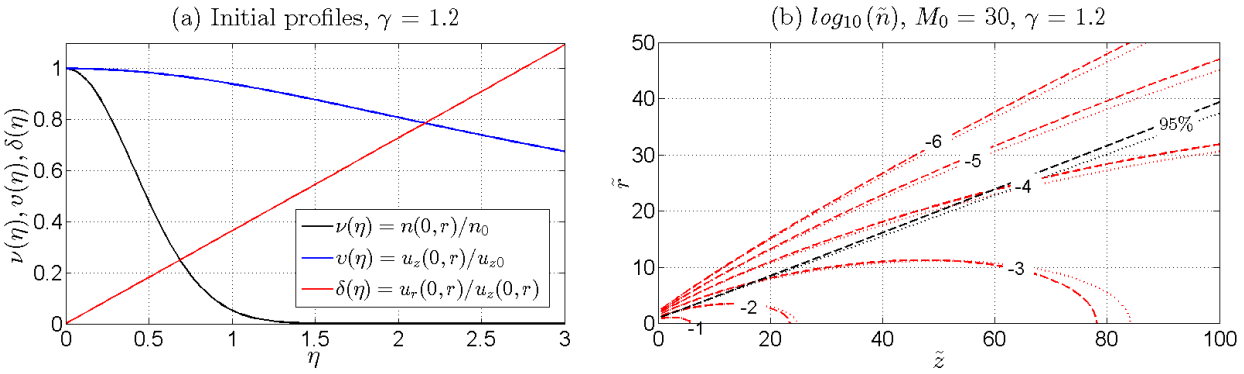

Figure 2. (a) Initial normalized profiles for density, axial velocity and divergence for $\alpha_0 = 20$ deg, $\gamma = 1.2$, a Gaussian density profile and a conical velocity field. (b) Corresponding plasma density (red lines) and 95% ion current streamlines (black lines) for a $M_0 = 30$ flow for both the zeroth (dotted line) and first order (dashed line) solutions.

A. Convergence Region of the Method

In order for the method to be applicable, the series expansion of Eq. 16 must converge. A necessary condition for this is that $\varepsilon\tilde{u}_{zi}^{(i+1)}$, $\varepsilon\tilde{u}_{ri}^{(i+1)}$ and $\varepsilon\ln\tilde{n}^{(i+1)}$ be absolutely smaller than $\tilde{u}_{zi}^{(i)}$, $\tilde{u}_{ri}^{(i)}$ and $\ln\tilde{n}^{(i)}$ by a given factor F^i beyond a certain i. A quantitative criterion to evaluate the convergence region can then be expressed particularizing this condition for $i = 0$ with $F^0 = 1$, i.e. $\varepsilon|\ln\tilde{n}^{(1)}| < |\ln\tilde{n}^{(0)}|$ for what regards the density perturbation.

Fig. 3 (a,b,c) shows the value of the first-order perturbations (stripped of the ε factors) for several initial divergence angles $\alpha_0 = 10$, 20, 30 deg and cooling rates $\gamma = 1.0$ and 1.2. The same initial profiles of Fig. 2(a) have been used. As expected, it is found that the three perturbations are generally larger for small initial divergence angles and lower γ values. This effect is caused by the larger initial divergence growth in a plume which is low divergent. The fact that the perturbations grow monotonously and unbounded downstream (at least for the $\gamma = 1$ case) means that the solution is not uniformly valid everywhere, but only within a finite region of validity that depends on the Mach number M_0, the initial profile, and the cooling rate. Visibly, the largest perturbation is on the density, with values as large as 1500 at $\eta = 1$ in the example shown, Fig. 3(c). Fig. 3 (d) displays the convergence region contour lines of the first order solution for $M_0 = 5$, 10, 20, 30, $\gamma = 1.0$ and $\alpha_0 = 20$ deg. The validity region is the area under the plotted lines. Clearly, the higher M_0, the wider the convergence region of the method. It is pointed out that, even within the convergence region of the method, the accuracy might be very poor and additional terms in the expansion could be required. However, it is possible to increase both the accuracy and the convergence region extension by re-initializing

the method at a plane sufficiently close to the initial one, where perturbations have not grown so much as to require additional expansion terms.

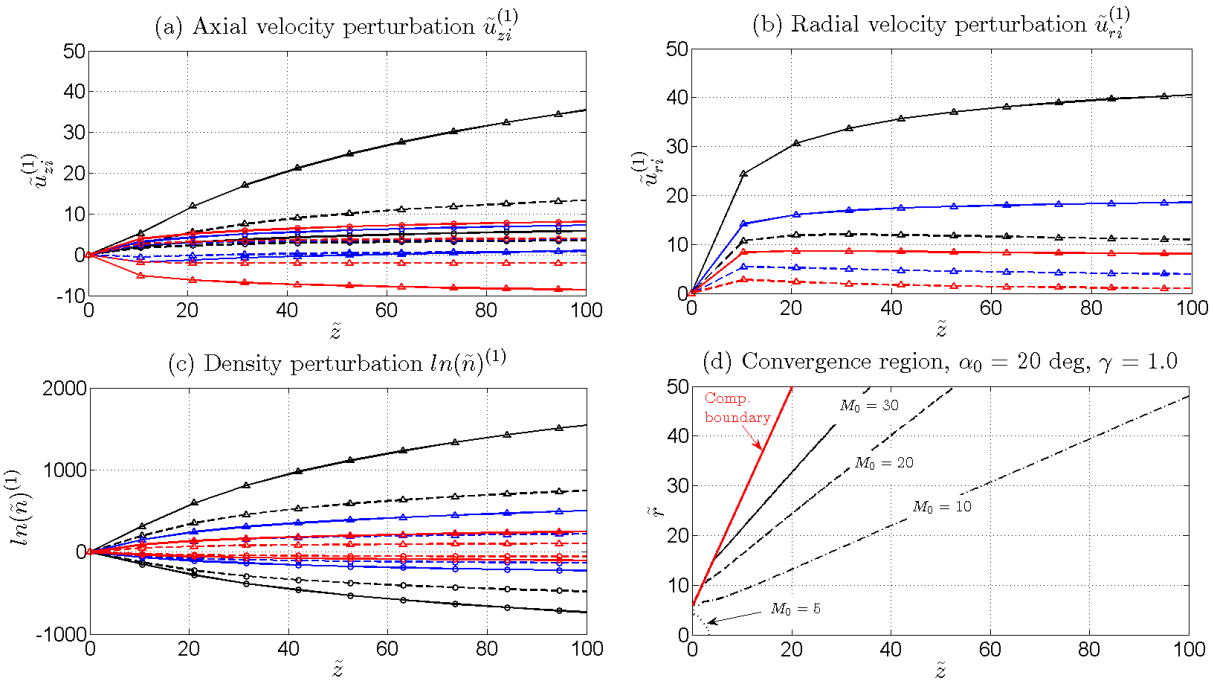

Figure 3. First order perturbations in axial velocity (a), radial velocity (b) and density logarithm (c) for $\gamma =$ 1.0 (solid lines) or 1.2 (dotted lines), $\alpha_0 = 10^o$ (black), 20^o (blue) or 30^o (red) and for the centerline (circles) and the $\eta^0 = 1$ streamline (triangles). Convergence region (d) for $\alpha_0 = 20$ deg, for various Mach numbers: 5 (dotted line), 10 (dash-dot line), 20 (dashed line) and 30 (solid line) in the isothermal $\gamma = 1$ case. Criterion is: $\varepsilon|\ln \tilde{n}^{(1)}| < |\ln \tilde{n}^{(0)}|$. No AEM re-initialization has been applied here.

IV. Self Similar Method

The self-similar method (SSM) approach, described in detail in Ref. 8, starts off by assuming that all the streamlines expand similarly, so that any of them is expressed as:

$$\tilde{r}_i\,(\eta,\zeta) = \eta h(\zeta), \tag{21}$$

where η, initial streamline radius at $\zeta = 0$, is used (again) to label the streamlines and $h(\zeta)$ (with $h(0) = h_0 = 1$) is a self-similarity or dilation function to be determined. Then, the initial plasma profiles $\nu(\eta)$, $\upsilon(\eta)$ are simply propagated in ζ with two scaling functions:

$$\tilde{n} = \nu(\eta)\tilde{n}_c(\zeta), \tag{22}$$

$$\tilde{u}_{zi} = \upsilon(\eta)\tilde{u}_c(\zeta), \tag{23}$$

with $\tilde{n}_c(0) = \tilde{u}_c(0) = 1$. Note that the functions $\tilde{n}_c$ and $\tilde{u}_c$ reflect the evolution of density and velocity along $\eta = 0$ (the 'centerline', hence subindex 'c'). Derivation with respect to time in Eq. (21) leads to the following basic relation between the velocity components:

$$\tilde{u}_{ri} = \tilde{u}_{zi}\eta h', \tag{24}$$

and particularization at $z = 0$ reveals a first constraint on the initial plasma profile, $\delta = \eta h_0'$ (i.e., an initially conical velocity profile), a restriction that has to be fulfilled in order to allow self-similar solutions.

Using Eqs. (22) and (23) in the continuity equation Eq. (9) leads to:

$$h^2\tilde{n}_c\tilde{u}_c = 1 \tag{25}$$

while the radial momentum equation Eq. (11) can be separated in ζ and η as:

$$M_0^2 \frac{h\tilde{u}_c \left(\tilde{u}_c h'\right)'}{\tilde{n}_c^{\gamma-1}} = C \tag{26}$$

$$-\frac{\nu^{\gamma-2}\nu'}{\eta \upsilon^2} = C, \tag{27}$$

where C is a separation constant. Eq. (27) establishes a ligature between ν and υ, the second constraint on the initial plasma profile for the SSM to be applicable, from which it is apparent that ν must satisfy $\nu' \leq 0$ for all η. The integration constant C is univocally determined by the curvature of the density profile at $\eta = 0$, since $\upsilon(0) = 1$ and $\nu(0) = 1$:

$$C = -\frac{d^2\nu}{d\eta^2}(0) \tag{28}$$

This means that the lower the value of C, the more radially expanded the initial profile. In practice, ν (and C) can be tuned so that the $\eta = 1$ streamline contains 95% of the total ion current (as we did in Sec. III). Fig. 4 (a) shows the dependence of υ and of ν on the value of γ, when a Gaussian density profile $\nu = \exp\left(-C\eta^2\right)$ is chosen. The axial velocity profile υ is strongly affected by the γ value, as a higher cooling rate causes a faster radial reduction of this velocity. Finally, the δ profile is completely unaffected by the γ value and retains its conical shape, which is a necessary condition for the SSM.

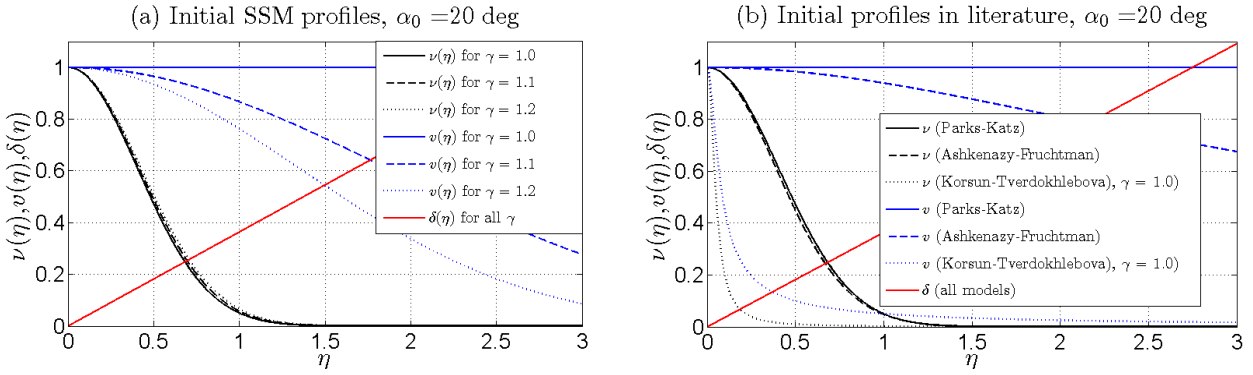

Figure 4. SSM initial profiles: dependence on γ (a) for a Gaussian density profile. Initial profiles considered by several authors (b). Ashkenazy-Fruchtman profile has been obtained with the choice $k = \tan^2(\alpha_0)$.

So far, we have two equations, Eq. (25) and (26) to determine the three unknowns h, $\tilde{n}_c$ and $\tilde{u}_c$. The third and last equation should come from the axial momentum equation Eq. (10). Unfortunately, trying to apply the same approach to it leaves us with an expression that cannot be separated in ζ, η:

$$\left(\tilde{u}_c^2\right)' - \tilde{n}_c^{\gamma-2}\tilde{n}_c' \frac{2C\eta^2}{M_0^2}\left(\frac{\nu}{\nu'\eta} - \frac{h'}{h}\frac{\tilde{n}_c}{\tilde{n}_c'}\right) = 0, \tag{29}$$

where Eq. (27) has been used to simplify the result. Moreover, Eq. (29) renders the system incompatible, since the second term cannot be made independent of η. This proves that no self-similar solutions of this type exist strictly, and provides a means to measure the local error committed by the SSM at any point as the residual ϵ_l of Eq. (29). Therefore, in order to proceed with the derivation of the approximate SSM, we need to discard Eq. (29) and replace it with an appropriate condition.

A. SSM Methods with $\tilde{u}_c = 1$

A convenient choice to replace Eq. (29) in the case of hypersonic plasma plumes is the approximation:

$$\tilde{u}_c = \text{const} \equiv 1, \tag{30}$$

which is justified by the size of the error in Eq. (29), proportional to $1/M_0^2$ and therefore vanishing for $M_0^2 \gg 1$. The function $\tilde{n}_c$ then follows immediately from Eq. (25):

$$\tilde{n}_c = 1/h^2, \tag{31}$$

and Eq. (26), now $h^{2\gamma-1}h'' = C/M_0^2$, can be integrated to provide the self-similarity function h, using the transformation $h'' = h'\mathrm{d}h'/\mathrm{d}h$:

$$(h')^2 - (h'_0)^2 = \frac{C}{M_0^2} \times \begin{cases} -\left(h^{2-2\gamma} - 1\right)/(\gamma - 1) & \text{for } \gamma > 1, \\ 2\ln h & \text{for } \gamma = 1. \end{cases} \tag{32}$$

The final integration step can be carried out numerically (or analytically in the isothermal case, in terms of the error function erf). Solving for h immediately yields the streamlines of the expansion. Note that only in the non-isothermal case does the streamline slope have an asymptotic value downstream, that is $(h')^2 \to (h'_0)^2 + 1/(\gamma - 1)$.

Lastly, the local error Eq.(29) can be written compactly as:

$$\epsilon_l = \frac{C}{M_0^2} \frac{h'}{h^{2\gamma-1}} \left(4\eta \frac{\nu}{\nu'} + 2\eta^2\right), \tag{33}$$

showing that ϵ_l is only zero for initial plasma profiles with $\nu \propto \eta^{-2}$, which unfortunately have an unphysical infinity near $\eta = 0$. The only degrees of freedom, besides the parameters M_0 and γ, are the value of h'_0 and the initial plasma profile, for which only one between ν or υ can be fixed independently. Parks and Katz[23], Korsun and Tverdokhlebova[24], and Ashkenazy and Fruchtman[25], independently developed three formulations of the SSM by applying additional hypotheses on the initial plasma profile, which can be regarded as particularizations of the general SSM framework derived here. In Ref. 23, $\gamma = 1$ and $\upsilon = 1$ are chosen, leading to a Gaussian density profile:

$$\nu = \exp\left(-C\eta^2/2\right), \tag{34}$$

which is depicted in Fig. 4 (a). The local error committed by this method cancels out for the streamline $\eta = \sqrt{2/C}$.

In Ref. 24 the choice is the following:

$$\nu = \left(1 + C\frac{\eta^2}{2}\right)^{-1}; \quad \upsilon = \left(1 + C\frac{\eta^2}{2}\right)^{-\gamma/2}, \tag{35}$$

which incidentally makes the local error independent of η, while in Ref. 25, υ and ν are established for the isothermal case $\gamma = 1$ as:

$$\nu = \left(1 + k\eta^2\right)^{-C/(2k)}; \quad \upsilon = \left(1 + k\eta^2\right)^{-1/2}, \tag{36}$$

where k is an arbitrary constant. In order to reproduce a perfectly conical velocity profile (constant total velocity at the initial plane), such constant can be chosen to depend on the initial divergence angle of the $\eta = 1$ ion current line: $k = \tan^2(\alpha_0)$. Similarly to the method of Ref. 23, the local error cancels out for a single streamline.

The density and velocity profiles of these three approaches are compared in Fig. 4 (b), after enforcing that 95% of the ion current be within the $\eta = 1$ streamtube. This condition causes Parks-Katz and Ashkenazy-Fruchtman profiles to have a similar appearance, whereas the profile from Korsun-Tverdokhlebova model separates substantially (due to a larger contribution to the flux integral in the plume periphery). Observe that Ashkenazy-Fruchman model becomes the isothermal version of Korsun-Tverdokhlebova model for $k = C/2$.

It is interesting to notice that the profile choice in SSM is not restricted to these three particularizations of the general case and that any profile that complies with Eq. (27) can be chosen. This can be used to try to better match a given initial density or momentum profile. Nevertheless, in order to independently define the density and velocity profiles, the AEM method presented in Sec. III should be used instead. Observe that the cold beam method described there is only self-similar when $\delta' = \text{const}$, i.e., for a pure conical expansion.

While the axial momentum equation Eq. (10) is essentially disregarded in the SSM making the error $\epsilon_l = O(M_0^{-2})$ for the $\tilde{u}_c = \text{const}$ case, the fact that the radial momentum equation Eq. 11 is fully satisfied yields a plume solution that reproduces quite accurately the main features of the hypersonic plasma expansion of a HET or a GIT. SSM methods have been successfully employed to propagate a known plume profile into the far-region, as done in Ref. 17.

As an example, Fig. 5 shows the density plot and the local error, $\log_{10}|\epsilon_l|$, for the Parks-Katz model for $\alpha_0 = 20$ deg and $M_0 = 10$. The h function or, equivalently in this paper, the 95% ion current line is displayed as well.

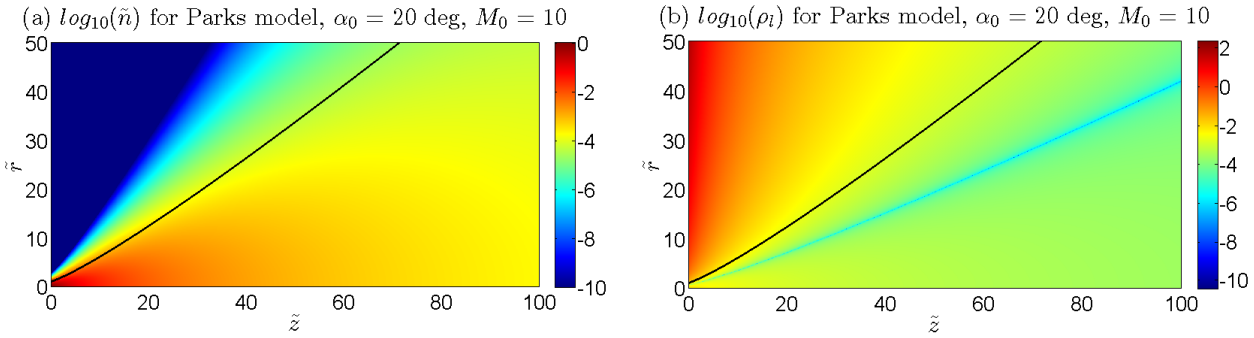

Figure 5. Density plot for the Parks-Katz model (a) and the corresponding local relative error in the axial momentum equation (b). The 95% ion current line is shown as a solid black line in both a) and b).

V. Comparison and discussion of the two approximations

A. Accuracy of the Methods

To allow the comparison of the two methods, the initial profile reported in Fig. 4 (a) will be considered in the following, as it is one permitted by the more restrictive SSM method. The δ profile will depend on the initial divergence angle α_0 considered in each case, according to the relation $\alpha_0 = \arctan(\delta(\eta = 1))$ and its direct proportionality with η (necessary condition for the SSM).

Fig. 6 (a), (b), (c) and (d) shows, for $\alpha_0 = 20$ deg and different combinations of M_0 and γ, the density contour lines and the $50 - 95\%$ ion current lines for the considered methods: zeroth (dotted lines), first order AEM (dashed line), SSM (dash-dot line) and MOC (solid line). It can be seen that both first order AEM and SSM agree well with the MOC solution in both density and streamlines prediction for $M_0 = 30$, while the first order AEM density solution departs significantly from the exact one for $M_0 = 15$, especially for an isothermal plasma. This is to be expected, as the lower Mach number brings nearer the limit of the convergence region of the AEM, thus penalizing its accuracy. A higher number of expansion terms would then be required.

Fig. 7 (a), (b), (c) and (d) shows, for the same cases as Fig. 6, the relative errors in density (black lines) and total velocity (red lines) with respect to the MOC solution for the different methods. Such errors are evaluated at the final plane $\tilde{z} = 100$ as a function of the radius. It can be appreciated that, at the centreline $\tilde{r} = 0$, the SSM density prediction is always better than the first order AEM, while the first order AEM predicts the total velocity better. For the cases with $M_0 = 15$, the first order AEM density error becomes larger than the zeroth order one at a sufficiently high radius. This is because the AEM method is far from converging in those cases and would need additional expansion terms or a re-initialization, as described in Sec. III, which has not been applied here.

Apart from the M_0 effect, the initial divergence angle α_0 also has a deteriorating effect on the first order AEM accuracy. Fig. 8 (a) and (b) shows the magnitude of the relative density estimation error (with respect to the MOC solution) at the plume centerline for $\tilde{z} = 100$ as a function of the initial Mach number and for various initial divergence angles. Two γ values are considered once again: 1.0 and 1.2. In all cases, the relative error clearly reduces with increasing Mach numbers, as expected. In both γ cases, for the SSM the relative error is never higher than 3%. The accuracies of the two methods start to become comparable for Mach numbers above 20 ($\gamma = 1.2$ case) and above 30 ($\gamma = 1.0$ case). For the AEM, the accuracy always increases with both the initial divergence angle and the γ coefficient. These effects are obvious, since the higher the α_0 and the γ, the closer the solution is to the cold conical one. In any case, the second order AEM solution, not discussed here, should further improve the solution. Regarding the SSM, on the other hand, the accuracy increases only slightly as the initial divergence angle decreases and γ increases. The influence of such parameters on its accuracy is nevertheless quite small.

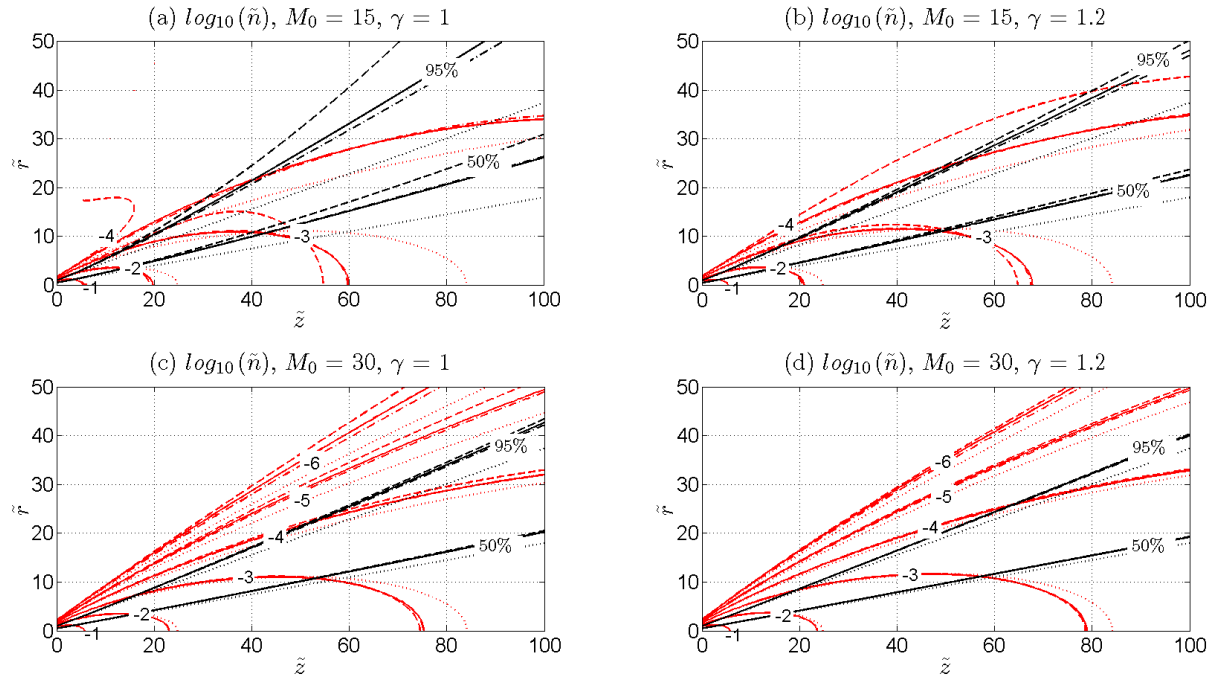

Figure 6. Density contour plot (red lines) and 50-95% ion current lines (black lines) for $\alpha_0 = 20$ deg and different combinations of M_0 and γ: (a) $M_0 = 15$, $\gamma = 1$, (b) $M_0 = 15$, $\gamma = 1.2$, (c) $M_0 = 30$, $\gamma = 1$, (d) $M_0 = 30$, $\gamma = 1.2$. Different methods are shown: AEM zeroth order (dotted lines), AEM first order (dashed lines), SSM (dash-dot lines) and MOC (solid lines).

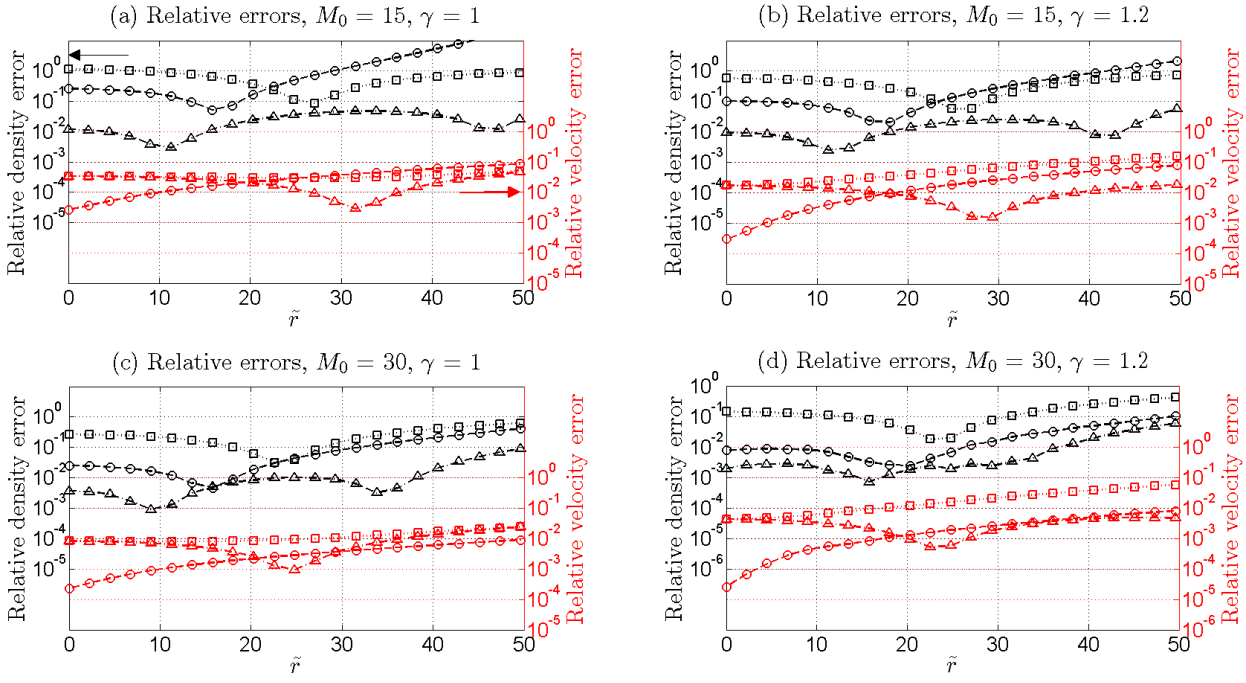

Figure 7. Relative errors with respect to the MOC solution in density (black lines) and velocity (red lines) at $\tilde{z}$=100 as a function of the radius. Different combinations of M_0 and γ are considered: (a) $M_0 = 15$, $\gamma = 1$, (b) $M_0 = 15$, $\gamma = 1.2$, (c) $M_0 = 30$, $\gamma = 1$, (d) $M_0 = 30$, $\gamma = 1.2$. Different methods are shown: AEM zeroth order (squares), AEM first order (circles) and SSM (triangles).

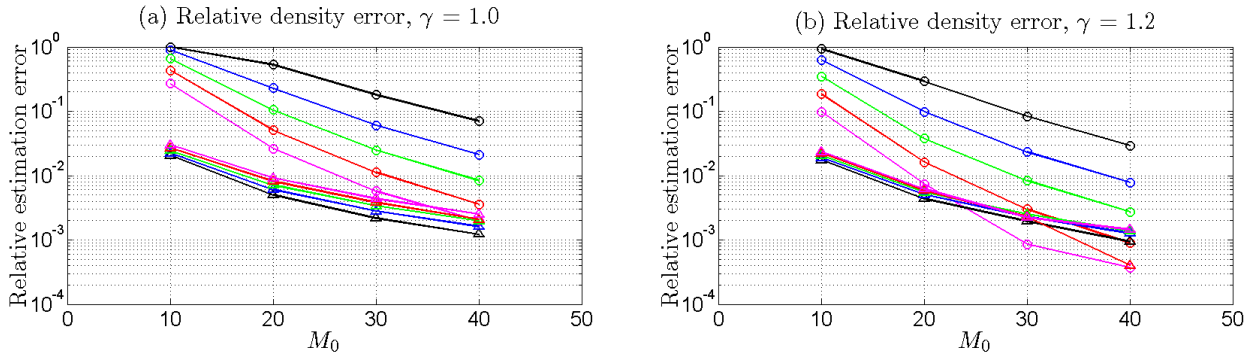

Figure 8. Relative error in the density estimation at $\tilde{z} = 100$, $\tilde{r} = 0$ for $\gamma = 1.0$ (a) and 1.2 (b) for both the first order AEM (circles) and the SSM (triangles). $\alpha_0 = 10$ deg (black lines), 15 deg (blue lines), 20 deg (green lines), 25 deg (red lines), 30 deg (magenta lines).

B. Far Field Divergence Angle

We define the *equivalent* far field divergence angle as:

$$\alpha_F(\tilde{z}_f) = \arctan\left(\frac{\tilde{R}_b(\tilde{z}_f) - 1}{\tilde{z}_f}\right) \tag{37}$$

where $\tilde{R}_b(\tilde{z}_f)$ is the normalized radius of the 95% ion current streamline at a distance $\tilde{z}_f$ from the thruster, which we will take here to be $\tilde{z}_f = 100$.

α_F is a very important figure of merit of the plume expansion, since it describes the minimal cone that always contains 95% of the ion current up to $\tilde{z}_f$. Such equivalent divergence angle may be used in a preliminary design of a large orbital platform, to choose the appropriate relative positions of the electric thruster and sensitive surfaces that might be damaged by the plume itself. Furthermore, in the IBS perspective, such angle can be used to determine very quickly, the momentum transfer efficiency (ratio between force transmitted to the target debris and the thrust force of the electric thruster) as a function of the operating S/C-debris distance, as done in Ref. 2. The formulation presented there can be easily generalized to a non-conical plume by using this equivalent far field divergence angle in place of the initial divergence angle.

Regarding the physics affecting the value of the far field divergence angle, three are the main parameters to consider. First of all, as advanced in Sec. II, the Mach number has the strongest impact on the radial beam expansion. Increasing the Mach number, by either achieving a faster plume or a lower electron cloud temperature, has the clear effect of reducing the radial expansion due to thermal effects.

Secondly, the initial divergence angle affects the far field divergence angle, as it obviously sets its minimum value. In the cold beam limit, the two angles, α_F and α_0, are exactly the same as the plume can be treated as a perfectly conical beam.

Lastly, the effective electron cooling rate, here modeled through γ, has a great influence as well, as a faster cooling reduces the pressure effects downstream. The closer to 1 is γ, the higher the radial expansion will be and, for the same M_0 and α_0, the higher the far field divergence angle.

The far field divergence angle as a function of M_0 and α_0 for $\gamma = 1$ and 1.2 is shown in Fig. 9 (a) and (b).

The contour lines for a cold conical beam would be horizontal lines, i.e. the far field divergence angle would be exactly equal to the initial divergence angle α_0. The presence of a radial expansion due to thermal electron pressure, makes the iso-lines of the far field divergence angle deviate significantly from straight horizontal lines especially at low Mach numbers. The SSM and AEM methods, respectively represented by red and blue lines, provide very similar results for the far field divergence angle for $M_0 > 20$ and $\gamma = 1.2$, while for $\gamma = 1$ it is necessary to go up to $M_0 > 35$ to achieve similar results. The AEM method is out of its convergence region in the lower left section of the plot in both Fig. 9 (a) and (b) (low α_0 and M_0) and hence the far field divergence angle is not shown there.

An important conclusion is that at relatively low M_0 and α_0, the final divergence angle is essentially dictated by the Mach number, and the initial divergence angle has a minimal role in it. Hence, in order

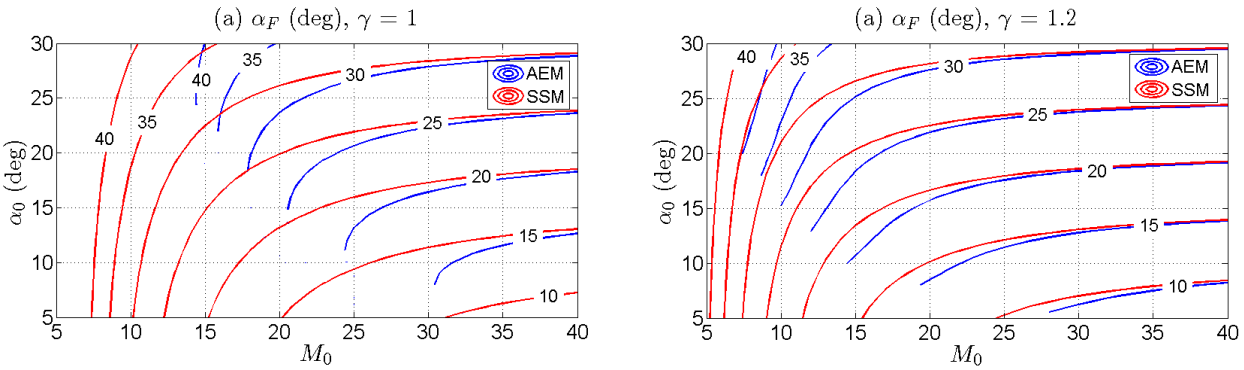

Figure 9. Far field divergence angle contour plot for $\gamma = 1$ (a) and $\gamma = 1.2$ (b), calculated using the two approximated methods: AEM first order (blue lines) and SSM (red lines). AEM first order solution shown only when within its convergence region.

to achieve very low far field divergence angles it is more appropriate to go for high M_0 rather than trying to achieve lower α_0. It is also observed that as $M_0 \to \infty$, the far field divergence angle approaches the initial divergence angle asymptotically, as one would expect. Lastly, a direct comparison of Fig. 9 (a) and (b), shows that the far field divergence angle is higher for the $\gamma = 1$ case at a given M_0 and α_0. As already commented, this is due to the fact that the electron pressure decays slower in this case thus yielding a higher integrated effect on the plume divergence.

VI. Development Status of the EP2-Plus Tool

While the most important physical effects of the far region plume may be addressed with semi-analytical methods, such as the ones described in this paper, the study of the physics occurring in the near region cannot be treated with a fluid model and generally requires particle codes.

Apart from near region effects such as momentum exchange collisions or electric/magnetic fields effects, there are other phenomena that cannot be tackled easily with fluid models.

First of all, the effect of an external magnetic field which might be non-axially symmetric makes the problem much harder to solve. Korsun, in Ref. 26, suggests that the effect of an oblique magnetic field can significantly deform the cross section of the plume, which is compressed in the direction normal to the magnetic field and the plume velocity vector and elongated in the other direction. Studying this problem is crucial in order to design an IBS mission, as the momentum transfer efficiency might change considerably with respect to that achieved by an axially symmetric beam. The plasma response, including the induced magnetic field generated by azimuthal plasma currents[8] , can play an important role in the total deformation.

From an IBS technique perspective, it is also very important to characterize the beam interaction with the target debris and other S/C surfaces, thus permitting to evaluate back-sputtering effects, the plasma potential bridge between S/C and target and the consequences of S/C and target charging. Note that a fine characterization of the lateral region of the plume, which is necessary to study the above effects, is not possible with the semi-analytical methods described in this paper, as they present increasing errors as we get farther away from the beam centerline.

With these issues in mind, the Plasmas and Space Propulsion Team (EP2) at *Universidad Carlos III de Madrid*, has started the development of a specialized 2D/3D hybrid-PIC code, EP2-Plus (*Extensible Parallel Plasma PLUme Simulator*) in order to study the plume expansion in a vacuum and its interaction with external magnetic fields, target and S/C surfaces. The heavy species (singly charged ions, doubly charged ions and neutrals) are thus treated as particles, while electrons are solved as a fluid, taking into account Maxwell's equations, in which the terms containing time derivatives are neglected. An interesting aspect of this code is the capability of simulating electrons as particles for short periods of time, to update the transport coefficients used in the fluid formulation. Moreover, the code must carefully deal with the reduction of particle number per cell as the expansion takes place by renormalizing the particle distribution in phase space, thus minimizing the statistical noise downstream while maintaining the accuracy of the simulation. Some of the primary simulation goals are listed below:

- Near region plume physics: electric potential, plasma density and backscattering effects due to momentum exchange collisions
- Effects of external oblique magnetic fields like the geomagnetic field
- Plume interaction with either a target debris or the S/C surfaces (solar panels, sensors, thruster ...)
- Non-axisymmetric emitters such as the neutralizer of HETs or GITs
- Multiple heavy species such as ions, neutrals and doubly charged ions

The EP2-Plus tool is being designed as an ensemble of 3 independent units that can be run separately: EP2-Plus SET to generate the simulation inputs, EP2-Plus CORE to simulate the real physics and EP2-Plus POST to postprocess the results. The files used as interface between the three units are of HDF5 format in order to boost the tool compatibility with other post-processing utilities available on the market. A high level structure of the whole tool is finally reported in Fig. 10 (a), while the computation loop performed by the numerical core is reported in Fig. 10 (b) and described below.

At every time step, particles are created (e.g. emission from a certain boundary or ionization), then destroyed (e.g. exit from the computational domain or destruction of an electron-ion pair due to recombination) and tracked (to reduce the computational effort of the following steps). Collisions are then simulated with a direct simulation Montecarlo (DSMC), which has the advantage of conserving both energy and momentum, as compared to a Montecarlo collisions method (MCC). After the collisions simulation, particles are weighted at the domain grid points to compute the ion current and density, which are the main inputs to a fields-solver algorithm, which computes the electron currents (quasi-neutrality is assumed) and the self-generated electric and magnetic fields. Only then, the fields are interpolated at the particles positions and these are advanced one time step, following a standard leap frog approach.

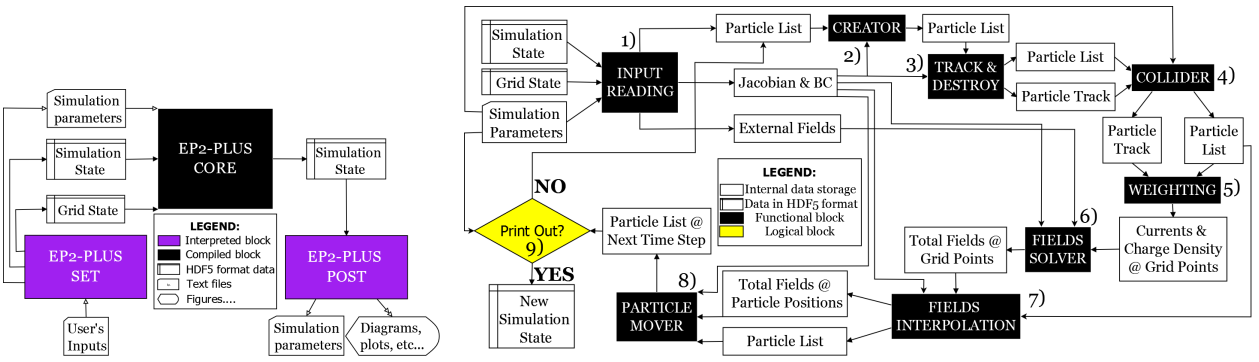

(a) Overall architecture of the EP2-Plus tool

(b) Functional scheme of the EP2-Plus CORE unit

Figure 10. EP2-Plus overall architecture (a) and block scheme of the CORE unit (b)

VII. Conclusions

We have presented two approximated solutions (Asymptotic Expansion Method, AEM, and Self-Similar Method, SSM) to the two-fluid, quasi-neutral, collisionless expansion of a plasma plume from a plasma thruster into vacuum. Such methods are of great interest for fast preliminary design in plume applications such as the Ion Beam Shepherd space debris deorbiter. The methods have been critically analyzed and discussed, using the 'exact' numerical solution obtained with the method of characteristics (MOC) to assess their accuracy and validity.

Both the AEM and SSM methods present some advantages and disadvantages. The AEM method enables more flexibility in the choice of initial density and velocity profiles (the only condition being $\delta, \delta' \geq 0$), allowing us to study complex or exotic plumes such as the hollow-cone plume of the HEMPT[27], which presents negative density gradients along the initial plane. This characteristic is not shared by the SSM, because of the ligature between density and velocity profiles represented by Eq. 27. Furthermore, no negative initial density gradient is allowed in the SSM, as this would lead to unphysical initial velocity profiles. An

additional advantage of the AEM is that the perturbation terms themselves are independent of ε and can be re-used to explore the effect of different Mach numbers on the expansion without recalculating the solution each time. The same cannot be said for the self-similar method, whose solution needs to be re-computed for each Mach number. The SSM, however, provides the ion streamline functions directly as part of the solution (function h).

Regarding the accuracy, both methods yield very accurate approximations for high M_0. Of course, theoretically, the AEM should permit to achieve better accuracies by adding more terms of the expansion within its convergence region. For the SSM, on the other hand, the solution cannot be easily corrected beyond $1/M_0^2$ accuracy without abandoning the self-similarity assumption. A clear disadvantage of the AEM, when compared with the SSM, is its narrow convergence region and its first order accuracy, which is quite worse at low Mach number and especially for isothermal plumes ($\gamma = 1$). However, such disadvantage can be avoided, at the cost of a more complex algorithm, by re-initializing the AEM method at subsequent initial planes, thus extending the convergence region and increasing the accuracy.

The main parameters of the expansion are the initial ion Mach number, M_0, the initial divergence angle, α_0, and the effective cooling rate, here modeled through γ. The three parameters (plus the initial plasma profile) fully determine the far field divergence angle: the Mach number condensates the effect of the electron pressure on the radial expansion. A lower Mach number means a higher pressure effect with respect to the ion inertia and thus a larger increase of the divergence. The cooling rate also affects the increase in divergence, in the sense that the higher the γ the lower the radial expansion of the beam. Lastly, the initial divergence angle sets a minimum value to the far field divergence.

Certain phenomena of great interest in both the near and far region plume cannot be easily tackled with models based on the fluid assumption. To address these shortcomings, an advanced hybrid/PIC code named EP2-Plus (*Extensible Parallel Plasma PLUme Simulator*) is being developed. The overall tool architecture and a short description of the simulation loop carried out by the numerical core has been reported as well.

Acknowledgments

The research leading to the results of this paper has been carried out within the *LEOSWEEP* project and has received funding from the European Union Seventh Framework Programme (FP7/2007-2013) under grant agreement N.607457.

References

[1]C. Bombardelli and J. Peláez. Ion beam shepherd for contactless space debris removal. *Journal of Guidance, Control, and Dynamics*, 34(3):916–920, May 2011.

[2]C. Bombardelli, H. Urrutxua, M. Merino, E. Ahedo, and J. Peláez. Relative dynamics and control of an ion beam shepherd satellite. In James V. McAdams, David P. McKinley, Matthew M. Berry, and Keith L. Jenkins, editors, *Spaceflight mechanics 2012*, volume 143 of *Advances in the Astronautical Sciences*, pages 2145–2158. Univelt, 2012.

[3]C. Bombardelli, M. Merino, E. Ahedo, J. Peláez, H. Urrutxua, and A. Iturri-Torrea† J. Herrera-Montojo†. Ariadna call for ideas: Active removal of space debris ion beam shepherd for contactless debris removal. Technical report, 2011.

[4]C. Bombardelli, H. Urrutxua, M. Merino, E. Ahedo, and J. Peláez. The ion beam shepherd: A new concept for asteroid deflection. *AA*, 90(1):98 – 102, 2013.

[5]M. Ruiz, I. Urdampilleta, C. Bombardelli, E. Ahedo, M. Merino, and F. Cichocki. The fp7 leosweep project: Improving low earth orbit security with enhanced electric propulsion. In *Space Propulsion 2014*, Cologne, France, 2014.

[6]A.G. Korsun, E.M. Tverdokhlebova, and F.F. Gabdullin. Simulation of plasma plume-to-spacecraft interaction. *Computer physics communications*, 164(1):353–364, 2004.

[7]H.B. Garrett. The charging of spacecraft surfaces. *Reviews of Geophysics*, 19(4):577–616, 1981.

[8]M. Merino, E. Ahedo, C. Bombardelli, H. Urrutxua, and J. Peláez. Hypersonic plasma plume expansion in space. In *32nd International Electric Propulsion Conference*, number IEPC-2011-086, Fairview Park, OH, 2011. Electric Rocket Propulsion Society.

[9]M. Merino, E. Ahedo, C. Bombardelli, H. Urrutxua, J. Peláez, and Leopold Summerer. Space debris removal with an ion beam shepherd satellite: Target-plasma interaction. In *47th AIAA/ASME/SAE/ASEE Joint Propulsion Conference*, number AIAA-2011-6142, Washington DC, 2011. AIAA.

[10]R.M. Myers and D.H. Manzella. Stationary plasma trhuster plume characteristics. In *23rd International Electric Propulsion Conference, Seattle, WA*, IEPC 93-096, 1993.

[11]M.R Nakles L. Brieda, W.A Jr Hargus D. R. Garrett, and R.L. Randy. Experimental and numerical examination of the BHT-200 Hall thruster plume. In *43rd AIAA/ASME/SAE/ASEE Joint Propulsion Conference & Exhibit*, Washington DC, 2007. AIAA.

[12]J. Navarro, M. Martinez-Sanchez, and E. Ahedo. Collisionless electron cooling in a magnetic nozzle. In *50th AIAA/ASME/SAE/ASEE Joint Propulsion Conference*, Cleveland, Ohio, 2014. AIAA.

[13]J. Wang and Y. Hu. Fully kinetic simulations of mesothermal plasma expansion. In *13th Spacecraft Charging Technology Conference*, number 197, 2014.

[14]B.E. Beal, A. Gallimore, and J.M. Haas W.A. Hargus. Plasma properties in the plume of a hall thruster cluster. *Journal of Propulsion and Power*, 20(20):985 – 991, 2004.

[15]J.E. Foster, G.C. Soulas, and M.J. Patterson. Plume and discharge plasma measurements of an nstar-type ion thruster. In *36th Joint Propulsion Conference and Exhibit, Huntsville, Alabama*, 2000.

[16]B.E. Beal, A. Gallimore, and W.A. Hargus. Plasma properties downstream of a low-power hall thruster. *Physics of plasmas*, 12(123503):1, 8, 2005.

[17]K. Dannenmayer, S. Mazouffre, E. Ahedo, and M. Merino. Hall effect thruster plasma plume characterization with probe measurements and self-similar fluid models. In *48th AIAA/ASME/SAE/ASEE Joint Propulsion Conference & Exhibit*, number AIAA 2012-4117, Atlanta, Georgia, 2012. AIAA.

[18]E. Ahedo and M. Merino. Two-dimensional supersonic plasma acceleration in a magnetic nozzle. *Physics of Plasmas*, 17:073501, 2010.

[19]E. Ahedo and M. Merino. On plasma detachment in propulsive magnetic nozzles. *Physics of Plasmas*, 18:053504, 2011.

[20]C. Charles, R. Boswell, and M.A. Lieberman. Xenon ion beam characterization in a helicon double layer thruster. *Applied Physics Letters*, 89:261503, 2006.

[21]E. Ahedo and J. Navarro. Helicon thruster plasma modeling: Two-dimensional fluid-dynamics and propulsive performances. *Physics of Plasmas*, 20:043512, 2013.

[22]M. Merino and E. Ahedo. Plasma detachment in a propulsive magnetic nozzle via ion demagnetization. *Plasma Sources Science and Technology*, 23:032001, 2014.

[23]DE Parks and I. Katz. A preliminary model of ion beam neutralization. In *14th International Electric Propulsion Conference*, Fairview Park, OH, 1979. Electric Rocket Propulsion Society.

[24]A.G. Korsun and E.M. Tverdokhlebova. The characteristics of the EP exhaust plume in space. In *33rd AIAA/ASME/SAE/ASEE Joint Propulsion Conference & Exhibit*, Washington DC, 1997. AIAA.

[25]J. Ashkenazy and A. Fruchtman. Plasma plume far field analysis. In *27th International Electric Propulsion Conference*, Fairview Park, OH, 2001. Electric Rocket Propulsion Society.

[26]AG Korsun, EM Tverdokhlebova, and FF Gabdullin. Mathematical model of hypersonic plasma flows expanding in vacuum. *Computer physics communications*, 164(1-3):434–441, 2004.

[27]K. Koch and M. Schirra. The hempt concept - a survey on theoretical considerations and experimental evidences. In *32nd International Electric Propulsion Conference*, number IEPC-2011-236, Wiesbaden, Germany, 2011. IEPC-2011-236.